Remote Sensing of Environment 250 (2020) 112046

Contents lists available at ScienceDirect

Remote Sensing of Environment

journal homepage: www.elsevier.com/locate/rse

Spatial and temporal patterns of land loss in the Lower Mississippi River Delta from 1983 to 2016

Samapriya Roy[a,*], Scott M. Robeson[a], Alejandra C. Ortiz[b], Douglas A. Edmonds[c]

[a] Department of Geography, Indiana University, Bloomington, United States of America
[b] Department of Geology, Colby College, Waterville, ME, United States of America
[c] Department of Earth and Atmospheric Sciences, Indiana University, Bloomington, United States of America

ARTICLE INFO

Keywords:
Land loss
Fragmentation
LISA
Fragstats
Google earth engine
Landsat

ABSTRACT

The Mississippi Delta in coastal Louisiana has some of the highest rates of land loss in the world. This land-loss crisis might become a global problem because most major deltas are expected to be vulnerable to land loss during the remainder of the 21st century and beyond. Despite this predicament, we do not understand how land loss in a deltaic environment proceeds in time and space. Here, we evaluate the spatial and temporal trends of land loss in the Lower Mississippi River Delta (LMRD) region using spatial statistics and landscape metrics. We used nearly 4800 Landsat images to construct a series of three-year cloud-free composites from 1983 to 2016. From these data, we created a stability index (SI), which is a dimensionless measure of the number of land-to-water transitions that a land pixel makes before being considered lost. Our results indicate that on the LMRD, 75% of land loss is a single transition from land to water, while about 25% of land pixels have two or more transitions before being considered lost. Using a local indicator of spatial association, we show that pixels with similar SI tend to cluster together. Single transition clusters (low SI) form elongated shapes, they are densely packed, and they are predominantly, but not always, found on marsh edges. On the other hand, multi-transition clusters (high SI) form square-like shapes, they are more fragmented, and they are usually found in marsh interiors. Our analysis further shows that the land-loss area within the spatial patches with both high and low stability is strongly related to the density of land patches and their shape (R^2 of 0.717 and 0.545 respectively). Our analysis suggests that land-loss pixels on the marsh edges undergo different temporal patterns of land loss compared to those in the marsh interior. We hypothesize that this arises because wave edge-erosion drives land loss on marsh edges, whereas subsidence-related flooding drives land loss in marsh interiors. The stability index provides a useful way to characterize the processes causing land loss.

1. Introduction

Deltas are found at the mouths of 40% of all coastal rivers (Caldwell et al., 2019) and cover a small portion of Earth's land surface, but they are home to some of the world's highest population densities and biodiversity (Austin, 2006; Ericson et al., 2006; Syvitski et al., 2009; Tessler et al., 2015). Despite the importance of deltas to ecological productivity and people's livelihoods, they are extremely vulnerable to land loss given their proximity to the sea. The land-loss problem is further exacerbated by human activities upstream; human-modified rivers and deltas through channelization and damming, which has decreased sediment delivery (Giosan et al., 2014). The decreased delivery of sediments to deltas, coupled with relative sea-level rise, has led to increased flooding and land loss in some major deltas (Newton et al., 2012; Renaud and Kuenzer, 2012; Syvitski et al., 2009).

Despite the potential value of deltas to ecological services and productivity, we lack a clear picture of spatio-temporal patterns of land loss (Blum and Roberts, 2012; Blum and Roberts, 2009; Day et al., 2007; Day et al., 2000; Lam et al., 2018; Ortiz et al., 2017), which limits our ability to mitigate the issue. The Lower Mississippi River Delta (LMRD) is an ideal place to study this problem because land loss has been on-going and is documented for nearly a century. The LMRD, from 1956 to 1990 has lost over 3400 km^2, or about 25%, of deltaic wetlands (Blum and Roberts, 2012; Blum and Roberts, 2009; Day et al., 2007; Day et al., 2000; Morton, 2003). The LMRD accounts for more than 30% of the coastal wetlands in the United States and has the fourth largest basin area and seventh largest water discharge in the world. The LMRD is one of the largest and most ecologically essential deltas in the world and serves as an ideal model for creating sustainable solutions to land loss.

* Corresponding author.
E-mail addresses: roysam@iu.edu (S. Roy), srobeson@iu.edu (S.M. Robeson), acortiz@colby.edu (A.C. Ortiz), edmondsd@iu.edu (D.A. Edmonds).

https://doi.org/10.1016/j.rse.2020.112046
Received 28 February 2020; Received in revised form 5 August 2020; Accepted 10 August 2020
Available online 25 August 2020
0034-4257/

Previous studies of land loss in the LMRD relied on hand-drawn maps, ground sampling, and early satellite data to constrain the magnitude of the problem (Britsch and Dunbar, 1993; Couvillion et al., 2011; Craig et al., 1979; Houck, 1983; Penland et al., 2000a). These early studies had a coarse temporal resolution and were able to define the first-order trend of changing land area through time. But, as we move toward designing sustainable solutions for the LMRD, we also need to understand patterns of land loss over decadal timescales. To create reliable decadal-scale estimates of land loss, we can take advantage of the improved capability to create time-series composites and perform parallelized operations on time stacks of imagery (Donchyts et al., 2016a, b; Hansen et al., 2014; Pekel et al., 2016) that produce more temporally consistent datasets.

Furthermore, most previous analyses did not consider the dynamic spatial and temporal nature of land loss (Britsch and Dunbar, 1993; Britsch and Dunbar, 1993; Couvillion et al., 2011; Penland et al., 2000b). Recently, the methods to detect the dynamic nature of land loss have improved considerably, especially with substantial improvements in cloud computing and the capability to analyze deep-time stacks of imagery (Donchyts et al., 2016a, b; Gorelick et al., 2017). Afterall, land loss is not instantaneous; in most cases, it can transition from land to water and back to land again over periods ranging from months or years due to yearly to decadal changes in water level (Olliver and Edmonds, 2017; Hiatt et al., 2019). Herein, we define two broad types of land loss: i) single-transition land loss occurs when land transitions once and becomes water for the remainder of the study period, and ii) multiple-transition land loss occurs when a parcel of land undergoes one or more land-to-water transitions before it is lost.

These two types of land loss are rarely separated in coastal studies of the LMRD and can provide clues into the processes driving land loss. For example, coastal erosion acts on marsh edges that are exposed continuously to waves and ocean currents (Bernier et al., 2006; Blum and Roberts, 2009; Britsch and Dunbar, 1993; Couvillion et al., 2016; Couvillion et al., 2011; Day et al., 2000; Kesel, 1989; Penland et al., 2000b). When viewed through time, coastal erosion is effectively instantaneous as land irreversibly becomes water. In contrast, the process of subsidence can occur anywhere within the delta, including more inland areas. Subsidence, though not always, is often slower than edge erosion and loss may be preceded by more frequent flooding (McKee and Cherry, 2009; Miller et al., 2008; Morgan, 1972; Wells, 1996).

In this paper, we develop a new approach to explore the spatial and temporal pattern of land loss in the Lower Mississippi River Delta (LMRD). Our methodology introduces the concept of a stability index as a measure of land-water dynamics as a temporal process rather than as a single event. In our study, we have defined land as lost only if it transitions from land to water and remains as water for at least the last two periods of observation. This method could be applied to any coastal environment that is experiencing land loss. We address three core research questions to examine the patterns of deltaic land loss in the LMRD from 1983 to 2016: 1) What proportion of land loss undergoes single versus multiple transitions? 2) Are single or multiple transition pixels spatially clustered or dispersed? 3) Do these spatial clusters have varying morphologies?

2. Material and methods

2.1. Study area and datasets

Our study area is the Lower Mississippi River Delta (LMRD), where we investigated watersheds at two different spatial scales (Fig. 1). Hydrological Unit Codes (HUCs) are designations by the United States Geological Survey (USGS), chosen to maintain consistency in the spatial scale of hydrological analysis. Within the LMRD, four HUC-6 watersheds are composed of 94 smaller HUC-12 watersheds (Fig. 1), with HUC-12 being the smallest designation assigned by USGS. We used coastal HUC-12 watersheds only, while avoiding large urban populations, resulting in modified HUC-6 watersheds being used for the analysis (Fig. 1). We exclude population centers because this study focuses on trying to link patterns to underlying natural processes and anthropogenic effects might influence these relationships.

To build a dataset with spatial and temporal consistency we use satellite imagery from Landsat missions, which serve as the longest historical and open-source satellite dataset in the world. With its 30-m resolution and 16-day repeat cycle, Landsat products provide a globally consistent spatial and temporal resolution (Hansen et al., 2014; Ju et al., 2012; Li and Roy, 2017; Roy et al., 2010). Given the size of the study area, multiple Landsat scenes were needed for each HUC-12. However, not all Landsat scenes are usable because clouds and cloud shadow obscure land (Donchyts et al., 2016a; Hansen et al., 2014; Hansen and Loveland, 2012; Roy et al., 2010). To minimize issues with cloud cover and short-term weather systems, such as hurricanes and storms that rapidly alter land morphology, we created three-year temporal composite imagery from using Landsat sensors (Chander et al., 2009; Chander and Markham, 2003; Donchyts et al., 2016b; Goward and Williams, 1997).

To generate the composite imagery, we evaluated nearly 4800 Landsat tiles, each of which has less than 30% cloud cover (Table 1). Each composite image is created from three years of Landsat scenes. Only TM and ETM+ are used to maintain spatial and spectral consistency (i.e., no MSS data are used). As Operational Land Imager (OLI) data from Landsat 8 was used in the final composite, we performed adjustments (Roy et al., 2016) to account for differences in sensing mechanism and spectral bands before combining them into a single image collection. All composites are for three years, except for the first period (1980 to 1983) when a limited number of images were available for our area of interest (Table 1).

Our composite images are created from orthorectified and calibrated top-of-atmosphere (TOA) reflectance scenes to correct for between-scene variations in solar irradiance (Chander et al., 2013; Chander et al., 2009; Chander and Markham, 2003) as used by others (Donchyts et al., 2016a; Dong et al., 2016; Goldblatt et al., 2016; Hansen and Loveland, 2012; Kuleli et al., 2011; Shelestov et al., 2017). The final step in creating multi-year composites is reducing the stack of images on a per-band per-pixel for each three-year period into a single image via a percentile reducer. The three-year period allowed us to remove extreme hydrological events, such as floods or high tides.

We use a percentile reducer on each three-year image collection to convert it to a temporal composite image. The percentile reducer uses the reflectance value corresponding to a user-defined percentile for each pixel (Fig. 2, Step 1). Percentile reducers generally perform better than a simple average because they are insensitive to outliers (Bornmann et al., 2013; Donchyts et al., 2016a, b; Pekel et al., 2016) and this method creates robust multi-year cloud-free composites (Donchyts et al., 2016a, b; Pekel et al., 2016). We use the 30th percentile value for each pixel because it performed well during composite creation (along with removing clouds and cloud shadows).

2.2. Land-water classification: spectral unmixing and K-means clustering

For each three-year composite image, we used spectral unmixing to determine the proportion of land or water in each pixel (Step 2, Fig. 2). As a soft classification technique, spectral unmixing allows for subpixel fractional abundance values of land or water classes for each pixel (Lu and Weng, 2007; Nath et al., 2014). To develop suitable land and water spectra, we collected endmember spectra from areas designated as permanent water and land bodies as designated by earlier global models (Donchyts et al., 2016a; Pekel et al., 2016). We used constrained spectral unmixing to make sure that the percentage of land or water for each pixel summed to one for each three-year composite (Keshava, 2003; Keshava and Mustard, 2002). We describe spectral unmixing using the linear mixing model (LMM) where we have M endmembers:

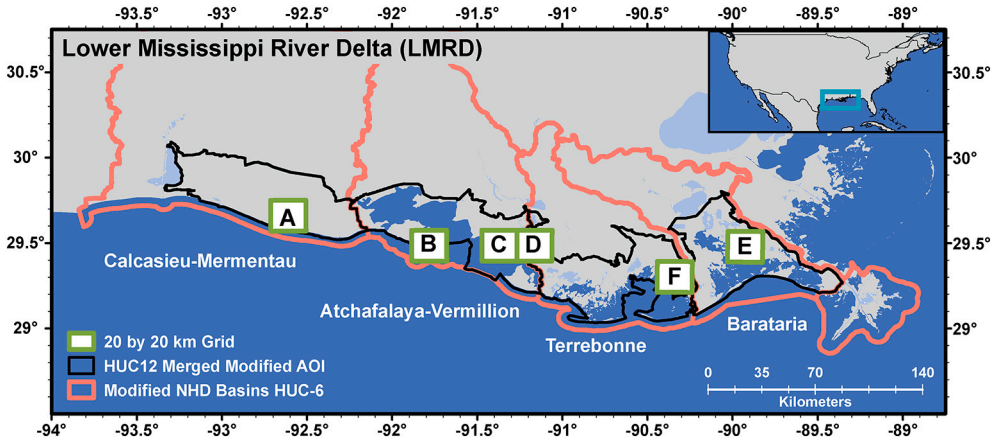

Fig. 1. Map of the Lower Mississippi River Delta showing large coastal watersheds (HUC 6 scale) that do not contain large urban areas. Red lines show the HUC-6 watersheds while the black lines show the coastal HUC-12 watersheds within each HUC-6 that form the area of interest. Boxes A-F show areas selected for further analysis within the overall basin. (For interpretation of the references to colour in this figure legend, the reader is referred to the web version of this article.)

Table 1
Landsat image count for image composites.

Start date	End date	# of images	Instrument type
1980-01-01	1982-12-31	56	Landsat TM
1983-01-01	1985-12-31	108	Landsat TM
1986-01-01	1988-12-31	269	Landsat TM
1989-01-01	1991-12-31	240	Landsat TM
1992-01-01	1994-12-31	276	Landsat TM
1995-01-01	1997-12-31	294	Landsat TM
1998-01-01	2000-12-31	503	Landsat TM & Landsat ETM+
2001-01-01	2003-12-31	636	Landsat TM & Landsat ETM+
2004-01-01	2006-12-31	648	Landsat TM & Landsat ETM+
2007-01-01	2009-12-31	606	Landsat TM & Landsat ETM+
2010-01-01	2012-12-31	514	Landsat ETM+
2013-01-01	2015-12-31	648	Landsat ETM+ & OLI

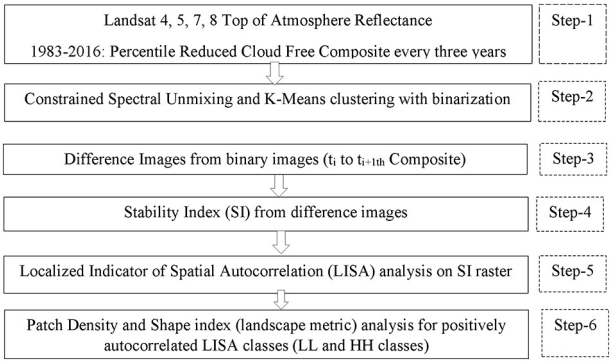

Fig. 2. Six-step workflow for the overall approach, leading from raw satellite data to landscape metrics in spatially autocorrelated geographic areas.

$$x = \sum_{i=1}^{M} a_i s_i + w = Sa + w$$

here x is the L by 1 spectrum vector, and S is the L by M matrix formed by the L endmembers, a is the fractional abundance (M by 1) for which we are solving, and w is the L by 1 additive observation noise vector (Keshava and Mustard, 2002). Since the images are temporal composites that are drawn from multiple dates over each three-year window and not a standard calibrated product from a single date, we use an adaptive percentile value composite that chooses a specific value for each pixel for the composite from the time stack. Hence, though linear spectral unmixing provides a percentage composition of each class and can be used for continuous measurement, a thresholding approach is needed with composites that are drawn from many different time slices (Liu and Yang, 2013; Nichol and Wong, 2007).

Unsupervised k-means clustering was applied to the percentage water to generate a single value threshold to binarize land and water. The result was a land-water binary map for each three-year period that we use to assess spatial patterns of land loss. Also, while validation is possible for single reference imagery, a composite image provides a unique validation challenge and cannot be compared to a standard high-resolution image because it is time-transgressive. The overall process was assembled as a series of scripts in Google Earth Engine.

2.3. Spatial disturbance and development of the stability index (SI)

In this paper, we introduce the concept of the stability index (SI) and apply it to the land-water binaries. Our stability index is inspired by the ecological theory that shows how ecosystems often iterate toward stability (Averill et al., 1994; Loreau et al., 2003; Marleau et al., 2014), which we measured using the relative frequency of a pixel transitioning between land or water states. Our SI is based on the observation that not all pixels undergo a single transition from land to water because some pixels transition multiple times between land and water. We calculate the number of transitions the pixel experiences prior to the final water conversion only on the subset of pixels that are considered lost. Because pixels can transition from land to water and back again, it is difficult to define when a pixel is considered to be lost. Our operational definition is that a pixel is considered lost if it transitions from land to water at any point in the study period, and/or also remains water for at least the last two composites. With this definition, a pixel would be classified as land loss if it transitioned to water in the third-to-last composite and remained water for the final two composites. In principle, that same pixel (or others for that matter) could possibly transition back to land again in future timesteps. If this occurs, we would incorrectly count the pixel as land loss. This is a source of uncertainty in our analysis, but we do note that less than 10% of land loss pixels are from the second-to-last timesteps, so even if this were to occur it is not the majority of the land loss pixels (Table 2).

To capture the transition of a pixel from land to water or vice versa, we created difference images by subtracting composite at time t from the next composite at time $t + 1$ (Fig. 2, Step 3). These transitions are used to calculate SI, which assigns a measure of the stability to land-loss pixels:

$$\mathrm{SI} = \frac{\mathrm{K}}{\begin{cases} \frac{n}{2} \; if \; n \; is \; even \\ \frac{n+1}{2} \; if \; n \; is \; odd \end{cases}} \quad \text{for K} > 0,$$

where K is the number of times a pixel changes from land to water and n is the number of difference images (here, $n = 11$ as we have 12 three-year composites). We posit SI is a measure of the inherent stability of a land pixel and its tendency to undergo transitions between land and

Table 2
Pixels undergoing land to water transitions for each composite relative to total number of lost pixels during 1983 to 2018 (column 2) and the proportion of those pixels that experience different transition numbers (columns 3–7). Last two time steps from 2010 to 2016 are not show because they are used to determine final pixel class as water.

Composite year	Land to water transitions relative to total (%)	Percentage for each transition number				
		1	2	3	4	5
1983–1986	13.39	100.00				
1986–1989	9.69	100.00				
1989–1992	8.17	88.14	11.86			
1992–1995	10.72	90.70	9.30			
1995–1998	9.70	83.50	16.44	0.06		
1998–2001	10.47	77.56	20.53	0.96		
2001–2004	8.05	77.11	21.13	1.76	0.00	0.00
2004–2007	20.01	77.01	20.24	2.71	0.04	0.00
2007–2010	9.81	75.08	20.99	3.59	0.30	0.008

water (i.e., its resistance to change from land to water). Therefore, a pixel with high SI experiences multiple transitions from land to water (i.e., it is stable in that it resists the transition), and pixels with low SI have a single transition from land to water. SI can obtain a maximum value of one, which would mean the pixel oscillates between land and water in every single time step. In this application, SI is not calculated for $K = 0$ because this represents a pixel that has remained either land or water throughout the entire period. It is important to note that SI does not quantify land to water transitions resulting from tidal or river flooding since these are events with small temporal footprints that we filter out during the process of creating the multi-year composites. Because our composites are every three years, a transition from land to water represents a fundamental shift to a different state (from land to water or water to land) across the three-year composites. This suggests to us that the transition reflects a longer-term change in the local environment of the pixel.

2.4. Spatio-temporal autocorrelation

Calculation of SI has the distinct advantage of collapsing the temporal changes from multiple time steps into a single image. From this single image, we can then measure the spatial autocorrelation of temporal dynamics using the SI values at each pixel. Moran's *I* is often used to measure the degree of spatial autocorrelation (Lam et al., 2018; Nagendra et al., 2004); however, it is a global measure that provides just one value for the entire landscape. Moran's *I* is further limited by the stationarity assumption that the statistical properties of the variable of interest do not change across the landscape (Cliff and Ord, 1970; Fotheringham, 2009; Griffith, 2006; Griffith, 1992; Ord and Getis, 2001), which is frequently not the case. As our goal is to clearly identify clusters of high and low land-loss stability, we used the local Moran's I as our Local Indicator of Spatial Autocorrelation (LISA) to better understand interactions at the relevant scale of the land-to-water conversion processes:

$$I_i = z(SI)_i \sum_j w_{ij} z(SI)_j$$

where I_i is the LISA index for pixel *i*, $z(SI)_i$ and $z(SI)_j$ are the stability indices for pixel *i* or *j* in standardized form, and w_{ij} is the spatial weight (here, we used inverse-distance weighting with Euclidean distances), with the summation across all other *j* pixels ($i \neq j$).

The LISA analysis using the local Moran's I generates an index of how similar the SI value for a pixel is relative to its neighbors (Anselin, 1995; Ord and Getis, 1995; Wulder and Boots, 1998). For each pixel's *I*, 95% confidence intervals allow us to evaluate the statistical significance of local spatial autocorrelation. Compared to other local measures of spatial autocorrelation (such as Geary's c), the local Moran's I more readily allows us to identify the way in which a pixel is similar or different from its neighbors. For instance, we calculate whether a local pixel has similarly high or low SI values relative to its neighbors (i.e., the type of statistically significant positive autocorrelation between a pixel and its neighboring pixels rather than just the occurrence of spatial autocorrelation). Specifically in our context, the local Moran's I will identify areas where high SI pixels are surrounded by high SI pixels (High-High autocorrelation, HH) and where low SI pixels are surrounded by low SI pixels (LL). Unlike other local autocorrelation methods, this method also identifies distinct types of dispersed spatial clusters where a high SI value was surrounded by low values (HL) or a low SI value pixel was surrounded by high SI value pixels (LH). In many applications, these dispersed arrangements are treated as a form of negative spatial autocorrelation and frequently are not analyzed in depth due to the low percentage of pixels in these classes and their complex spatial origin (Griffith, 2006; Griffith, 1992; Wulder and Boots, 1998). The percentage of area lost in each of the LISA classes was calculated for all HUC-12 watersheds.

2.5. Landscape metrics: spatial configuration and morphology

Landscape metrics have arisen as a method to quantify spatial heterogeneity and help to explain the relationship between process and patterns (Turner, 1989; Turner et al., 2001). Landscape patches for the LISA-derived cluster types (i.e., clusters of HH or LL pixels) served as the classes for the study. These determine the spatial distribution of pixels with high and low stability and their analysis using landscape metrics is used to measure their spatial configuration. We use Fragstats (v 4.2.1, developed by the Forest Science Department, Oregon State University) to quantify the configuration and morphology of landscape patch (Lin et al., 2015; Nagendra et al., 2004; Turner, 1989; Turner et al., 2001; Turner et al., 1993; Turner and Rao, 1990; Uuemaa et al., 2009). For each LISA-derived cluster, we calculate landscape metrics (Table 3) that quantify the degree of fragmentation (patch density) and the shape of land loss (shape index). This choice was also informed by studies where factor analysis was performed across a few of these metrics to identify landscape metrics that are strongly correlated (Riitters et al., 1995). Each metric was calculated using a no sampling approach applied to the LISA classes. We also chose these landscape metrics based on the resolution of the spatial unit (HUC-12) and the imagery, because the spatial resolution impact the metric values and interpretation (Lin et al., 2015; Nagendra et al., 2004; Turner et al., 2001; Turner et al., 1993; Turner and Rao, 1990; Uuemaa et al., 2009).

For both HH and LL LISA classes, we calculated the percentage area lost, which describes the area lost in each HUC-12 watershed relative to all area lost in that watershed. We then used this percent area lost metric to test how land loss varied by landscape metric across the HUC-6 watersheds. This was done using two separate linear regression

Table 3
Explanation of landscape metrics used: Patch Density and Shape Index.

Metric	Formula	Description & use
Patch density (PD)	$PD = \frac{NP}{A}$ NP = Number of Patches A = Total area of patches (m^2) PD is always > 0 but constrained by cell size.	Higher PD values indicate a greater number of patches within the same area. PD is an indicator of fragmentation.
Shape index	$Shape\ index = \frac{0.25\, p_{ij}}{\sqrt{a_{ij}}}$ p_{ij} = perimeter of patch ij (m) a_{ij} = square root of patch area (m^2) adjusted by a constant to adjust for a square standard	Shape index ranges from 1 to infinity. Shape index = 1 represents square patches and at higher values, patches become more irregular.

Table 4
Proportion of pixels undergoing different number of transitions for the overall area and each HUC-6 watersheds.

	Percentage of Pixels Undergoing Transition				
# of Transitions	Overall	Atchafalaya-Vermillion	Barataria	Calcasieu-Mermentau	Terrebonne
1	75.08	67.90	75.81	81.20	68.99
2	20.99	27.44	20.20	16.50	24.45
3	3.59	4.20	3.49	2.24	5.87
4	0.30	0.46	0.47	0.06	0.67
5	0.008	0.00	0.02	0.00	0.02

models for HH and LL classes. In the two models, the percent area is the response variable, and the two landscape metrics (Patch Density and Shape) are continuous predictors while the HUC-6 watershed is a categorical predictor variable. Individual t-statistics for each variable, as well as the F-statistic and adjusted r^2 for the full model, are reported as metrics of the goodness of fit. Patch density and Shape were log-transformed to meet assumptions of normality.

3. Results

3.1. Land loss

We define a pixel as land loss if it transitions from land to water at any point in the study period and also remains water for at least the last two composites. Our analyses showed that of all the land-loss pixels, 75% undergo a single transition from land to water, while 21% of the pixels undergo two transitions from land to water and the remaining 4% of the pixels undergo three or more transitions from land to water and back. (Table 4).

The total land loss from 1983 to 2016 was 1403.85 km^2 (Figs. 3 and 4). The loss includes those land pixels that transition from land to water at any given three year time period of 1983 to 2016 and remain water pixels for the last two periods of our observation (2010–2016).

Sudden increases in land loss that occurred in 2004–2007 are coincident with hurricanes Katrina and Rita (Barras, 2007). Though the impacts of single-year events and stochastic flooding are minimized by our methods, these events have a long-lasting effect that is captured in the 3-year image composites. All of the transitions from land to water, and water to land are presented in Table 2, where as the single transitions are captured in Table 3. Table 2 shows that single and multiple transition land loss is relatively steady in time, with the exception that transitions three or more times become more common later in the study period because these pixels require time to accumulate transitions.

Besides those events, the land loss is relatively steady across the overall study area (Fig. 3). In the individual watersheds, loss is more variable through time. Barataria is relatively steady, but Calcasieu-Mermentau (hereafter CalcMerm) shows more variability at different times, compared to the overall study area. Terrebonne and Atchafalaya-Vermilion (hereafter AtchVerm) are highly variable and show fluctuations from 1990 to 2000 that are not obviously present in other watersheds.

3.2. Spatial clustering

We found that the behavior of land loss pixels ranges from multiple transitions (high SI value) to single transitions (low SI value) (Table 4; Fig. 4). At the basin scale, CalcMerm and Barataria have the highest proportion of area lost in the LL class (Fig. 5a), closely followed by Terrebonne, while AtchVerm had the lowest amount of land loss. Most pixels are either in the HH or LL class, so the area lost in the HH class is inversely related to that in the LL class, with LL being dominant in most HUC-12 watersheds. We find a higher proportion of area lost that is HH class (Fig. 5b) in AtchVerm and Terrebonne while Barataria and CalcMerm have lower proportions.

To understand how land loss and LISA classes are related, we examined six smaller subsets in detail (Figs. 6 and 7). These subsets were selected using a grid size of 20 by 20 km^2 to represent land loss across all four HUC-6 watersheds, a varying degree of transitions, and the different LISA classes. The LISA analysis shows that most LL classes are either along shorelines or lake edges, as well as among fragmented land-water boundaries (Fig. 6). HH pixels tend to be more inland, away from the coastal edge. Since the landscape is highly fragmented in some areas, there are some isolated low and high values of SI that lead to the LH and HL class distribution (Fig. 6).

The pixels that experience single transitions tend to be located across coastal shorelines and lake edges (Panel B & C of Fig. 7). CalcMerm shows coastal areas with low SI values (Panel F of Fig. 7), and most pixels have one transition from land to water. Barataria shows that areas with lower SI values (Panel E of Fig. 7) are distributed across internal lakes and coastal edges. Terrebonne low SI along edges (Panel A of Fig. 7) and higher SI values are located more inland (Panel D of Fig. 7).

All watersheds show a mix of LISA classes with a mix of single and multiple transitions along with a substantial amount of HL and LH classes (Panel A and D of Fig. 8). For AtchVerm, we find LL clusters along coastal edges interspersed with some LL patches with HH clusters inland (Panel B, C of Fig. 8). CalcMerm has LL clusters along coastal and lake edges, and HH classes were clustered more inland (Panel F of Fig. 8), and Barataria shows areas with loss and lower SI values (Panel E of Fig. 8) distributed across internal lakes and coastal edges.

3.3. Land-loss morphology

The morphologies of clustered HH and LL LISA classes are different. The LL class tends to be clumped (low Patch Density value) while the HH class is more fragmented (high Patch Density value) (Fig. 9A). HH has lower Shape Index values owing to large fragmented patches in the HH class (higher patch density), with many of the patches being individual pixels (Fig. 9B).

The relationship between patch density and land fragmentation is key in examining landscape patterns that directly affect land loss. Shape index determines the complexity of the morphology created as a result of such fragmentation. This relationship between land loss and landscape metrics was analyzed using a multiple regression model between percentage area lost in LL and HH LISA classes and log-transformed variables landscape metrics (Patch Density and Shape Index). HUC 6 is a categorical variable; the model suggests that while land loss is related to shape and patch density, it does not depend on the location/site of the analysis.

We observe a strong positive relationship between land loss and both Patch Density and Shape, for both LL and HH based land loss. Interestingly, this is not sensitive to whether the loss undergoes single or multiple transitions because a positive relationship is observed for both LL and HH classes across the HUC 12 watersheds (Table 5).

4. Discussion

This study examines the overall land loss in the Lower Mississippi River Delta (LMRD) from 1983 to 2016 using Landsat data. The purpose of this study was twofold: to highlight the complexities inherent in robustly estimating land loss and to provide a means of combining spatial and temporal dimensions of loss using SI. The paper introduces the concept of SI to establish land-water transitions that occur in a natural pixel, before converting to water and being considered lost. The paper categorizes a lost pixel as one that transitions to water and remains as a water pixel for the last two time periods of the study. By studying land loss that undergoes multiple transitions, relative to a single transition, we can identify important clues about the underlying

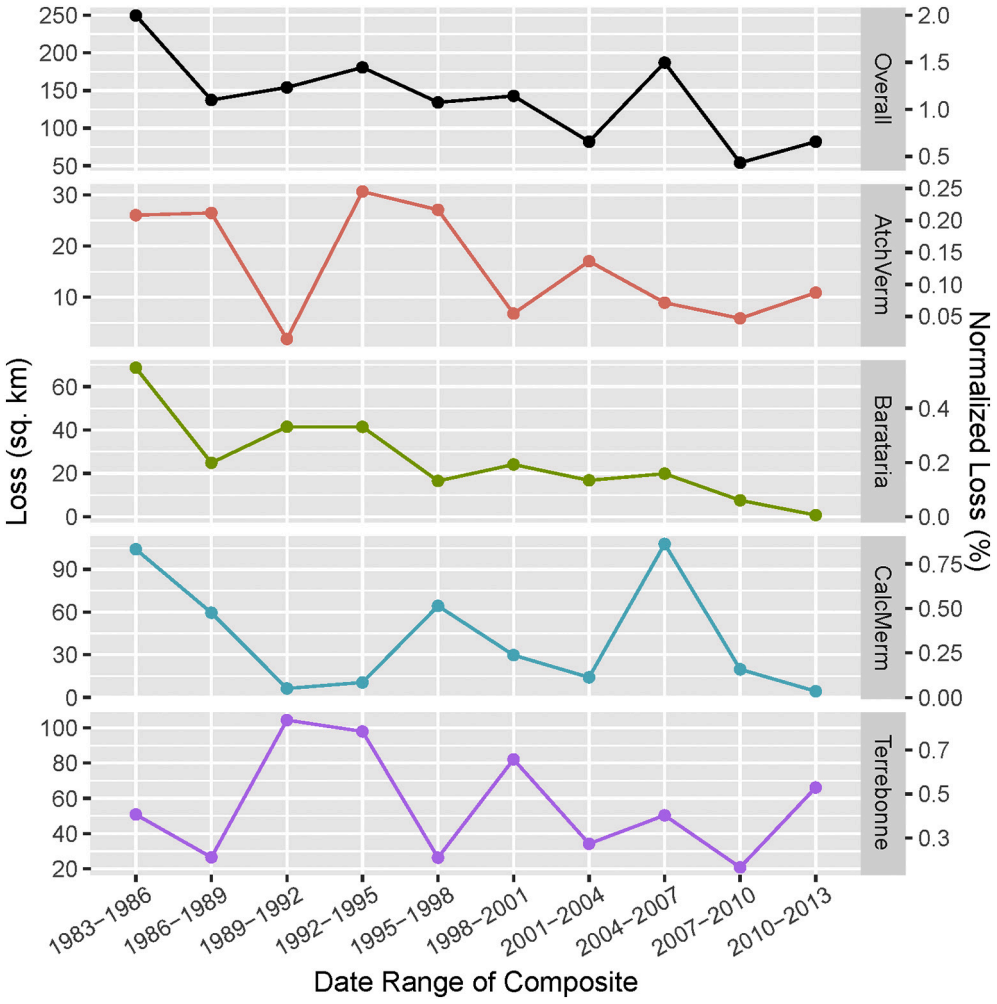

Fig. 3. Time series of land loss showing the area of land loss (left y-axis) and the area of land loss normalized by watershed area (right y-axis) that is lost in each time step and remains as a water class for the last two time steps. Since the 2013–2016 composite falls within the range determining loss, it is not included in the figure.

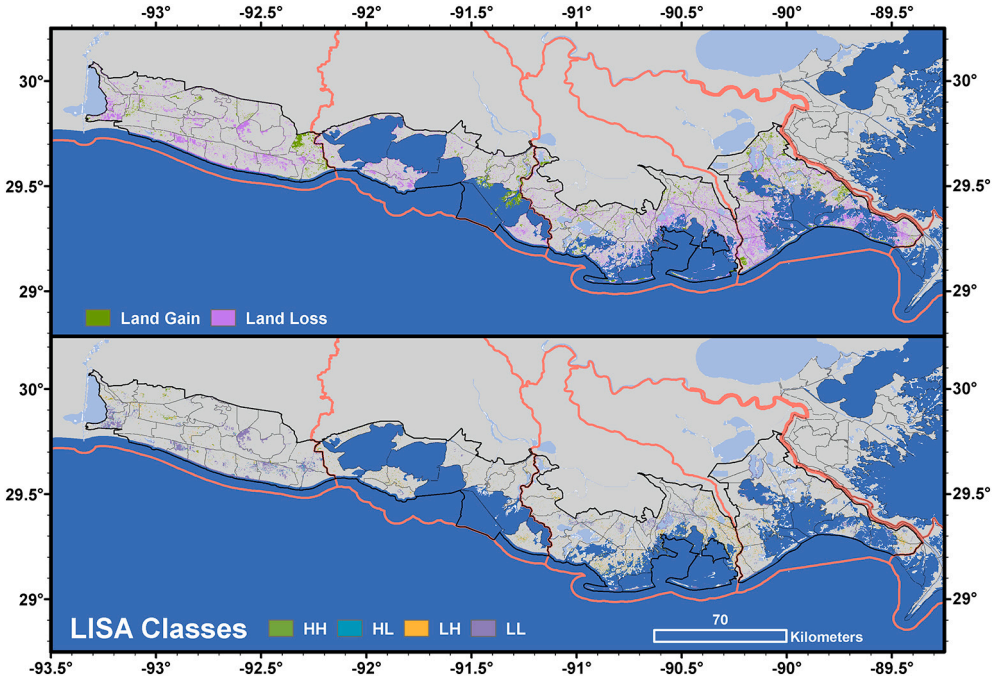

Fig. 4. Top: Overall land loss and land gain from 1983 to 2016. Bottom: LISA classes derived from SI.

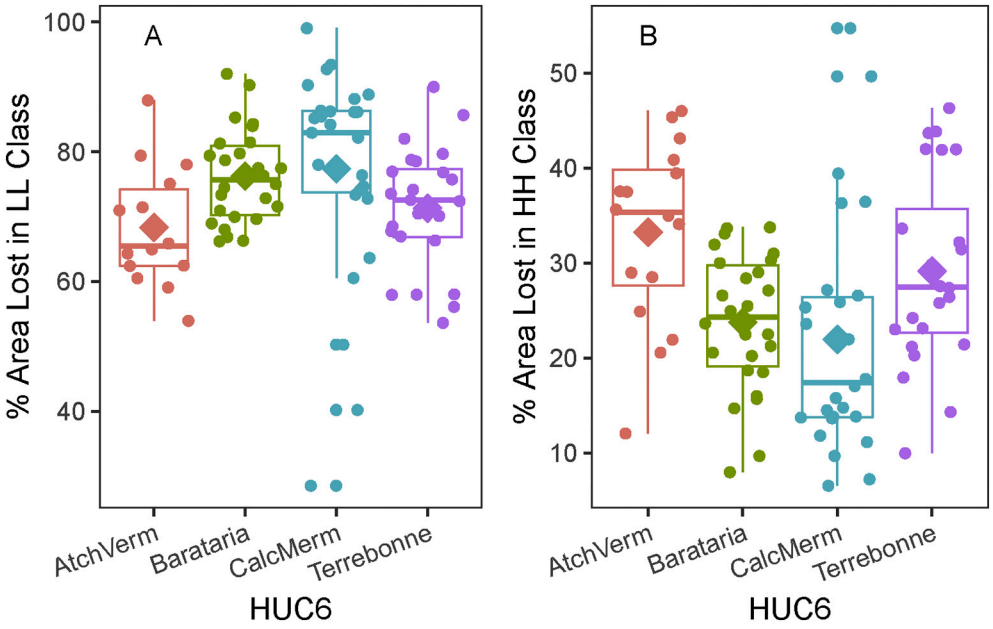

Fig. 5. Box plots of percentage area lost belonging to A) LL LISA Class and B) HH LISA class for each HUC-12 watershed within the four HUC-6 boundaries. Each circular point represents a single HUC-12 watershed and points are staggered along the x-axis for better viewing. The diamond represents the mean value of the distribution.

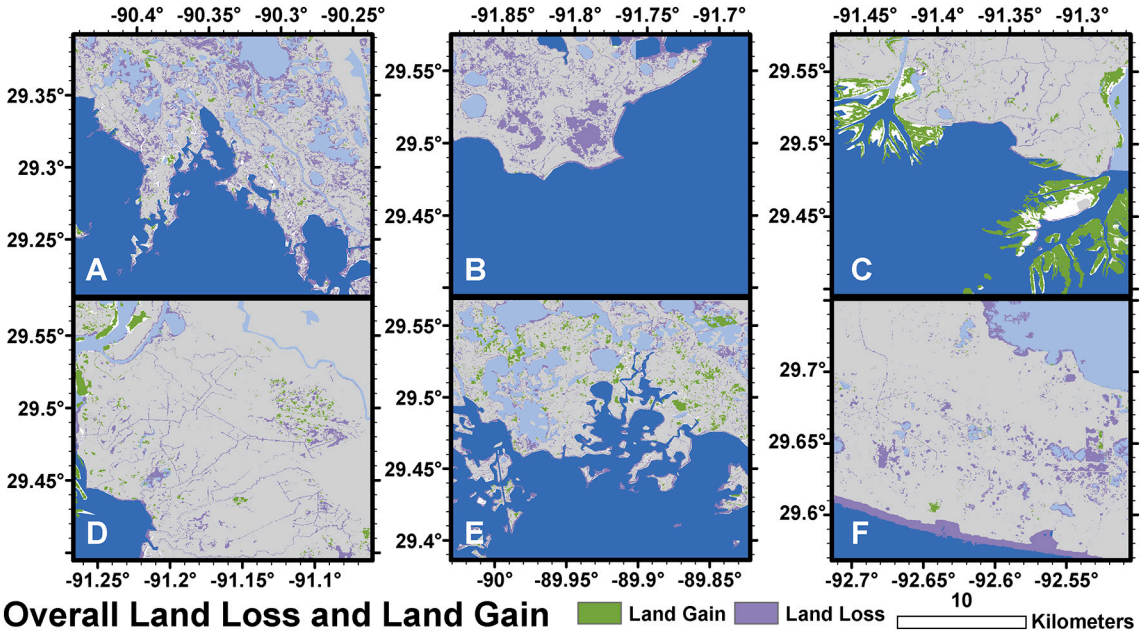

Fig. 6. Subareas of the LMRD (20 by 20 km) that depict representative patterns of land loss between 1983 and 2016 only. Panel A & D are from Terrebonne, Panels B, C are from AtchVerm, Panel E is in Barataria and Panel F is in CalcMerm (see Fig. 1 for locations). Gray areas represent land that did not experience land loss or gain, light blue represents inland perennial water, dark blue designates coastal waters, and white shading indicates areas where land and water are not classified. (For interpretation of the references to colour in this figure legend, the reader is referred to the web version of this article.)

processes driving land loss in delta environments. Our results demonstrate that though most land to water transitions occur as a single transition event (~75%), nearly 25% of the overall land area goes through two or more transitions between land and water before land loss.

Interestingly, our results show that different LISA classes are often clustered and have different shapes and functional characteristics. We hypothesize that the LL and HH LISA classes represent different processes that are driving land loss. For instance, the LL patches tend to have a low density and an elongated shape (Fig. 9); moreover, many of these patches are preferentially found on coastal and lake boundaries (Figs. 7, 8). Based on this pattern, and also the fact that most of these pixels undergo only a single transition from land to water, we suggest that they are primarily caused by wave edge erosion (Coleman, 1988; Day et al., 2000; Ortiz et al., 2017).

Consequently, the opposite is true for HH patches. The HH patches tend to have a high patch density, meaning that they tend to have more patches per unit area and are less concentrated. As a result of the high patch density, the shape index of each cluster is much lower (Fig. 9), indicating they have a geometrical shape that is square-like, and sometimes even represent just a single or limited number of isolated land pixels. These pixels are probably converted to water by subsidence or vegetation dieback (Nyman et al., 1994; Nyman and DeLaune, 1999) that can occur away from the marsh edge.

Our hypothesis that different land loss processes are associated with the different LISA classes requires field validation and more extensive

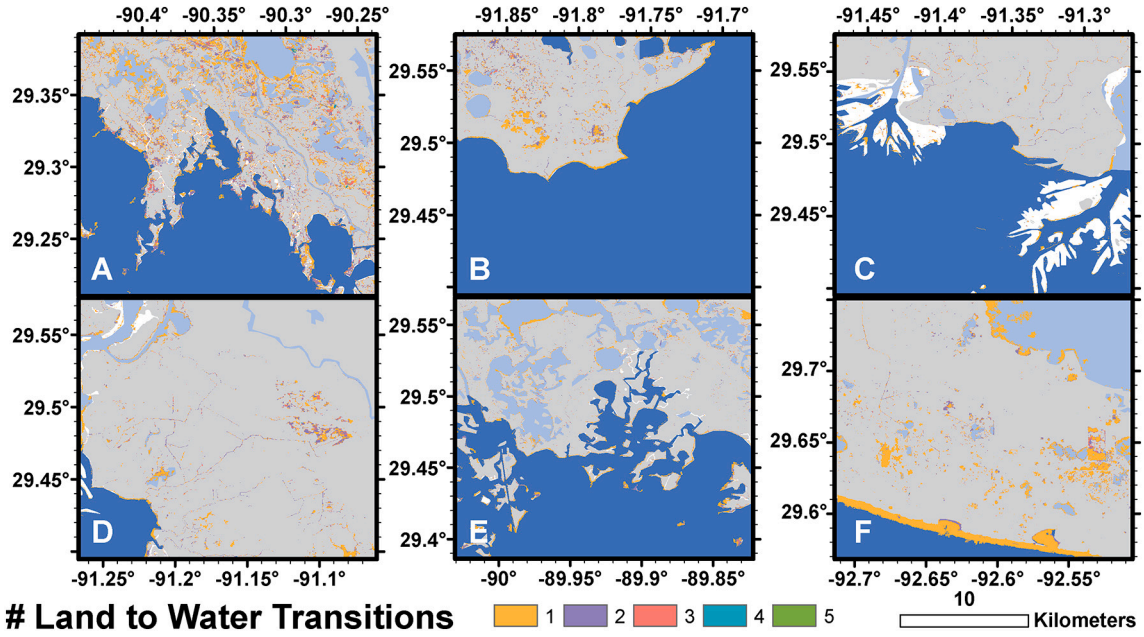

Fig. 7. Subareas of the LMRD (20 by 20 km) that show different land to water transitions. Panel A & D lies in Terrebonne, Panels B, C lie within Atchverm, Panel E lies in Barataria and Panel F lies in Calcmerm (see Fig. 1 for locations). The larger the number of transitions, the higher the stability index. Gray areas represent land boundaries, light blue represents inland perennial water and dark blue designates ocean boundaries, and and white shading indicates areas where land and water are not classified. (For interpretation of the references to colour in this figure legend, the reader is referred to the web version of this article.)

testing. Field validation and observations from high-resolution images would allow us to estimate the error of omission and commission for our classification schemes and land-to-water transitions. But, our compositing approach also makes ground truthing the multiple changes that have occurred over decadal timescales that much more challenging. Indeed, while our use of a series of multiyear composites over a 30+ year period is a feature of this work, it also is the reason why we were unable to provide precise error estimates for the image classifications.

But if our results are correct, it would suggest land loss in the LRMD is predominantly caused by edge erosion and/or rapid subsidence and flooding. LISA classes do not perfectly distinguish between land loss processes. For instance, LL patches, which predominantly occur on marshes edges can also occur far away from edges (see interior pixels in Fig. 8A,B,D,F). These interior LL pixels are not likely to be driven by wave edge erosion, but instead by rapid flooding and/or subsidence. Thus, if our interpretation of the LISA classes is accurate, it would suggest that roughly 75% of land loss on the LMRD is driven by wave

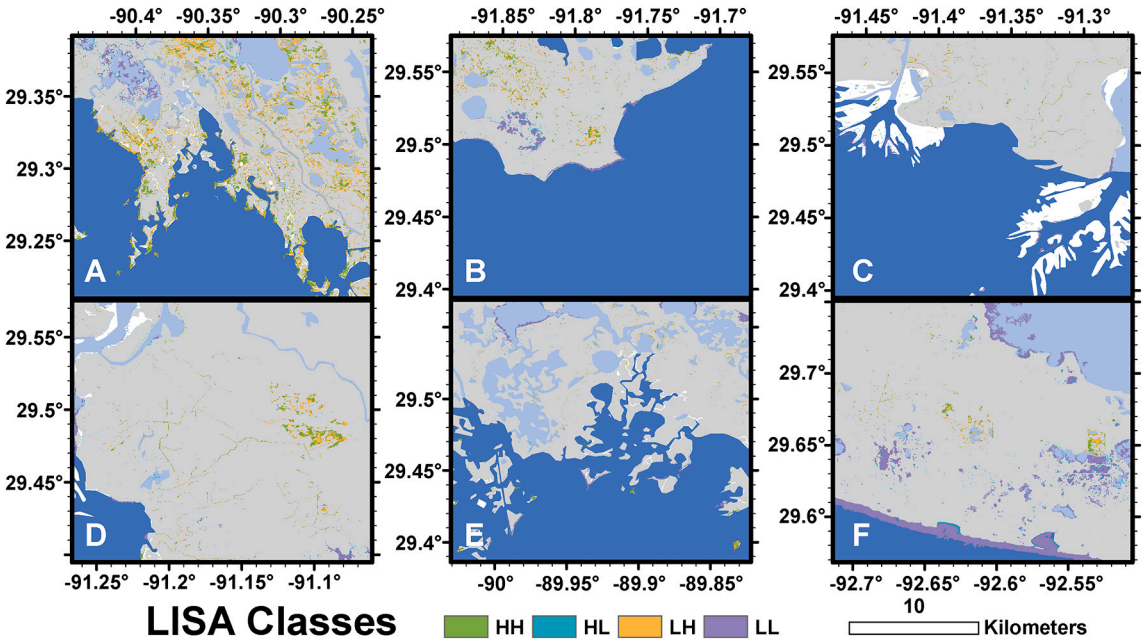

Fig. 8. Subareas of the LMRD (20 by 20 km) that depict cluster types, generated using the Local Indicator of Spatial Autocorrelation (see Fig. 1 for locations). The High-High (HH) and Low-Low (LL) values indicate positive autocorrelation versus HL and LH indicate spatial dispersion. Gray areas represent land boundaries, light blue represents inland perineal water and dark blue designates coastal waters, and and white shading indicates areas where land and water are not classified. (For interpretation of the references to colour in this figure legend, the reader is referred to the web version of this article.)

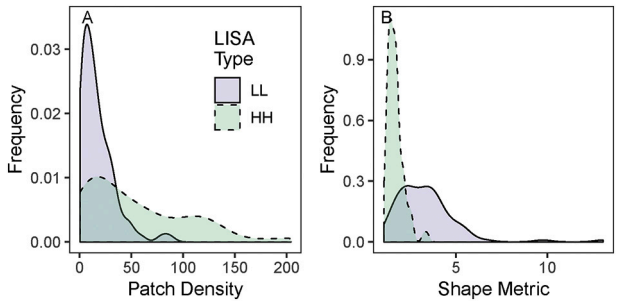

Fig. 9. Kernel density estimates of the distribution of (A) Patch Density for LL and HH type land loss classes and (B) Shape Index for LL and HH type land loss classes. The spatial metrics were calculated for HUC-12 watershed level.

edge erosion, and rapid flooding and/or subsidence. This provides a more nuanced interpretation than the recent analysis by Jankowski et al., 2017, who show, using the coastwide reference monitoring station (CRMS), that shallow subsidence is the primary driver of loss. Most of the CRMS data come from interior pixels, and for obvious reason, those stations are not placed on marsh edges. We suspect that the CRMS data oversample the interior parts of islands where wave edge erosion does not occur.

It is important to note that the processes of edge-erosion and subsidence do not act in isolation. For both the LL and HH patches, we see that land loss increases as land becomes more fragmented, which is measured by the multiple regression models for both LL and HH patches (Table 5). This could arise if subsidence or edge-erosion increases edge-length, thus providing more opportunities for erosion. The combination of these processes can create a positive feedback loop and accelerate land loss (Lam et al., 2018; Nagendra et al., 2004).

By studying the positively autocorrelated LISA classes, we were able to yield insights into the evolution of the delta environment more generally, and further show how LISA classes themselves may transition from one type to another as the landscape fragments. The use of both functional and spatial landscape metrics in the linear model provides evidence of a positive feedback loop between fragmentation and land loss. Delta processes such as subsidence, ponding, and sediment deposition change the landscape morphology and can then be interpreted using these landscape metrics as process proxies. For example, previous studies in coastal areas have linked Patch Density to patch isolation and ultimately land fragmentation, by identifying overall increases in marsh edges for wind and wave actions to have a detrimental effect (Kindlmann and Burel, 2008; Ortiz et al., 2017; Turner and Rao, 1990). In the LMRD, an example of this pattern would be the fact that newly formed small ponds often merge with larger ponds and increase land fragmentation, while simultaneously growing pond area via edge erosion and an increase in wind fetch (Ortiz et al., 2017).

We find that core area, which refers to land area in the patch, at a distance from the edge decreases (Haines-Young and Chopping, 1996; Luck and Wu, 2002; Neel et al., 2004; Tischendorf, 2001). As core area fragments, further edges get exposed to wave and wind action further accelerating fragmentation. We posit that the high values of patch density and shape index, which represents a fragmented landscape with more edges, might allow for multiple process regimes to deteriorate land. The paper demonstrates that land loss as a spatio-temporal process can be quantified using SI, which enables understanding the spatial and temporal trajectories of each pixel.

5. Conclusions

Deltas around the world are likely to experience land loss, but the driving causes of of land loss are hard to understand because of transitions between land loss and land gain. Our study provides a new spatio-temporal model to quantify the land loss and we use that model to hypothesize what processes drive patterns of land loss in the Lower Mississippi River Delta (LMRD). The new spatio-temporal model is sensitive to transitions between land and water, and on the LMRD 75% of land loss occurs by a single transition from land to water, while 25% of land loss experiences multiple transitions before becoming water. Single-transition loss pixels are clustered in space, have long, linear shapes, and are usually found along the shoreline. Multiple-transition pixels also are clustered in space, but have more compact shapes and are usually found in marsh interiors. Our data suggests that single-transition land loss is caused by wave-edge erosion, whereas multiple-transition land loss is caused by subsidence. Ultimately, field work will be helpful in better characterizing whether these classes are caused by subsidence or edge erosion, but the results hold promise for using long-term remote sensing information to determine processes of land loss. Moving forward, we think it is clear that the satellite record can provide a temporally rich depiction of the trajectory of land loss, including

Table 5
Multiple regression model results across HUC-12 watersheds using the land loss in low-low and high-high class as response variables. Log-transformed Patch Density and Shape Index are used as continuous predictors while HUC-6 watersheds act as categorical variables. Also contains the overall Adjusted R-squared, F-statistics, and *p*-value for both land loss in low-low and high-high class multiple regression model.

LISA class	Model terms	Estimate (± SE)	t-value	P-value
Low-low class (n = 95)	Intercept	47.98(± 3.27)	14.65	< 0.0001
	Patch density	6.41(± 0.76)	8.44	< 0.0001
	Shape	7.63(± 1.96)	3.89	0.0002
Adjusted R-squared = 0.545	HUC6-Barataria	3.99(± 2.73)	1.459	0.148
	HUC6-Calcmerm			
	HUC6-Terrebonne			
Overall F-statistic = 22.58		3.99(± 2.73)	1.289	0.201
Overall P-value < 0.0001		3.99(± 2.73)	0.859	0.392
High-high class (n = 95)	Intercept	-2.20(± 2.98)	-0.742	0.460
	Patch Density	6.78(± 0.54)	12.655	< 0.0001
	Shape	13.25(± 2.68)	4.937	< 0.0001
Adjusted R-squared = 0.716	HUC6-Barataria	-3.17(± 1.90)	-1.674	0.097
	HUC6-Calcmerm			
	HUC6-Terrebonne			
Overall F-statistic = 47.06		-1.13(± 2.10)	-0.536	0.593
Overall P-value < 0.0001		0.38(± 1.91)	0.198	0.843

single versus multiple transitions on a per-pixel basis.

Through this work, we have chosen to focus on a single region, the LMRD, but the approaches used here should be readily transferable to other delta systems. Only with an increased understanding of the diversity of ways that land is lost through time can we begin to build more predictive models for future climate change.

Declaration of Competing Interest

The authors declare that they have no known competing financial interests or personal relationships that could have appeared to influence the work reported in this paper.

Acknowledgements

S.R, A.C·O, and D.A.E. were supported by National Science Foundation grants 1426997 and 1812019. All data and code from this study are available from the corresponding author upon request. Because Google Earth Engine does not explicitly use version control, the code used in this manuscript may change as Earth Engine alogrithms and holdings are updated. The authors would like to thank the editor, Matt Hiatt, and one anonymous reviewers for critical comments that improved this manuscript. The authors would also like to thank Landon Yoder and Briana Whitaker for constant feedback in helping improve the manuscript.

References

Anselin, L., 1995. Local indicators of spatial association—LISA. Geogr. Anal. 27, 93–115.
Austin, D.E., 2006. Coastal exploitation, land loss, and hurricanes: a recipe for disaster. Am. Anthropol. 108, 671–691.
Averill, R.D., Larson, L., Saveland, J., Wargo, P., Williams, J., Bellinger, M., 1994. Disturbance Processes and Ecosystem Management. US Department of Agriculture, Forest Service, Washington, DC (19 p).
Barras, J.A., 2007. Satellite images and aerial photographs of the effects of Hurricanes Katrina and Rita on coastal Louisiana. Geological Survey (US).
Bernier, J.C., Morton, R.A., Barras, J.A., 2006. Constraining rates and trends of historical wetland loss. In: Mississippi River Delta Plain, south-central Louisiana. Coastal Environment and Water Quality. Water Resources Publications, Highlands Ranch, USA, pp. 371–382.
Blum, M.D., Roberts, H.H., 2009. Drowning of the Mississippi Delta due to insufficient sediment supply and global sea-level rise. Nat. Geosci. 2, 488–491.
Blum, M.D., Roberts, H.H., 2012. The Mississippi delta region: past, present, and future. Annu. Rev. Earth Planet. Sci. 40, 655–683.
Bornmann, L., Leydesdorff, L., Mutz, R., 2013. The use of percentiles and percentile rank classes in the analysis of bibliometric data: opportunities and limits. J. Inform. 7, 158–165.
Britsch, L.D., Dunbar, J.B., 1993. Land loss rates: Louisiana coastal plain. J. Coast. Res. 324–338.
Caldwell, R.L., Edmonds, D.A., Baumgardner, S., Paola, C., Roy, S., Nienhuis, J.H., 2019. A global delta dataset and the environmental variables that predict delta formation. Earth Surf. Dyn. Discus. 1–26. https://doi.org/10.5194/esurf-2019-12.
Chander, G., Markham, B., 2003. Revised Landsat-5 TM radiometric calibration procedures and postcalibration dynamic ranges. IEEE Trans. Geosci. Remote Sens. 41, 2674–2677.
Chander, G., Huang, C., Yang, L., Homer, C., Larson, C., 2009. Developing consistent Landsat data sets for large area applications: the MRLC 2001 protocol. IEEE Geosci. Remote Sens. Lett. 6, 777–781.
Chander, G., Hewison, T.J., Fox, N., Wu, X., Xiong, X., Blackwell, W.J., 2013. Overview of intercalibration of satellite instruments. IEEE Trans. Geosci. Remote Sens. 51, 1056–1080.
Cliff, A.D., Ord, K., 1970. Spatial autocorrelation: a review of existing and new measures with applications. Econ. Geogr. 46, 269–292.
Coleman, J.M., 1988. Dynamic changes and processes in the Mississippi River delta. Geol. Soc. Am. Bull. 100, 999–1015.
Couvillion, B.R., Barras, J.A., Steyer, G.D., Sleavin, W., Fischer, M., Beck, H., Trahan, N., Griffin, B., Heckman, D., 2011. Land Area Change in Coastal Louisiana from 1932 to 2010.
Couvillion, B.R., Fischer, M.R., Beck, H.J., Sleavin, W.J., 2016. Spatial configuration trends in coastal Louisiana from 1985 to 2010. Wetlands 36, 347–359.
Craig, N.J., Turner, R.E., Day, J.W., 1979. Land loss in coastal Louisiana (USA). Environ. Manag. 3, 133–144.
Day, J.W., Britsch, L.D., Hawes, S.R., Shaffer, G.P., Reed, D.J., Cahoon, D., 2000. Pattern and process of land loss in the Mississippi Delta: a spatial and temporal analysis of wetland habitat change. Estuar. Coasts 23, 425–438.
Day, J.W., Boesch, D.F., Clairain, E.J., Kemp, G.P., Laska, S.B., Mitsch, W.J., Orth, K., Mashriqui, H., Reed, D.J., Shabman, L., 2007. Restoration of the Mississippi Delta: lessons from hurricanes Katrina and Rita. science 315, 1679–1684.
Donchyts, G., Baart, F., Winsemius, H., Gorelick, N., Kwadijk, J., van de Giesen, N., 2016a. Earth's surface water change over the past 30 years. Nat. Clim. Chang. 6, 810.
Donchyts, G., Schellekens, J., Winsemius, H., Eisemann, E., van de Giesen, N., 2016b. A 30 m resolution surface water mask including estimation of positional and thematic differences using landsat 8, srtm and openstreetmap: a case study in the Murray-Darling basin, Australia. Remote Sens. 8, 386.
Dong, J., Xiao, X., Menarguez, M.A., Zhang, G., Qin, Y., Thau, D., Biradar, C., Moore III, B., 2016. Mapping paddy rice planting area in northeastern Asia with Landsat 8 images, phenology-based algorithm and Google earth engine. Remote Sens. Environ. 185, 142–154.
Ericson, J.P., Vörösmarty, C.J., Dingman, S.L., Ward, L.G., Meybeck, M., 2006. Effective Sea-level rise and deltas: causes of change and human dimension implications. Glob. Planet. Chang. 50, 63–82.
Fotheringham, A.S., 2009. "The problem of spatial autocorrelation" and local spatial statistics. Geogr. Anal. 41, 398–403.
Giosan, L., Syvitski, J., Constantinescu, S., Day, J., 2014. Climate change: protect the world's deltas. Nat. News 516, 31.
Goldblatt, R., You, W., Hanson, G., Khandelwal, A.K., 2016. Detecting the boundaries of urban areas in India: a dataset for pixel-based image classification in Google earth engine. Remote Sens. 8, 634.
Gorelick, N., Hancher, M., Dixon, M., Ilyushchenko, S., Thau, D., Moore, R., 2017. Google earth engine: planetary-scale geospatial analysis for everyone. Remote Sens. Environ. 202, 18–27.
Goward, S.N., Williams, D.L., 1997. Landsat and earth systems science: development of terrestrial monitoring. Photogramm. Eng. Remote. Sens. 63, 887–900.
Griffith, D.A., 1992. What is spatial autocorrelation? Reflections on the past 25 years of spatial statistics. L'Espace géographique 265–280.
Griffith, D.A., 2006. Hidden negative spatial autocorrelation. J. Geogr. Syst. 8, 335–355.
Haines-Young, R., Chopping, M., 1996. Quantifying landscape structure: a review of landscape indices and their application to forested landscapes. Prog. Phys. Geogr. 20, 418–445.
Hansen, M.C., Loveland, T.R., 2012. A review of large area monitoring of land cover change using Landsat data. Remote Sens. Environ. 122, 66–74.
Hansen, M.C., Egorov, A., Potapov, P.V., Stehman, S.V., Tyukavina, A., Turubanova, S.A., Roy, D.P., Goetz, S.J., Loveland, T.R., Ju, J., 2014. Monitoring conterminous United States (CONUS) land cover change with web-enabled Landsat data (WELD). Remote Sens. Environ. 140, 466–484.
Hiatt, M., Snedden, G., Day, J.W., Rohli, R.V., Nyman, J.A., Lane, R., Sharp, L.A., 2019. Drivers and impacts of water level fluctuations in the Mississippi River delta: implications for delta restoration. Estuar. Coast. Shelf Sci. 224, 117–137.
Houck, O.A., 1983. Land loss in coastal Louisiana: causes, consequences, and remedies. Tul. L. Rev. 58, 3.
Jankowski, K.L., Törnqvist, T.E., Fernandes, A.M., 2017. Vulnerability of Louisiana's coastal wetlands to present-day rates of relative sea-level rise. Nat. Commun. 8, 14792.
Ju, J., Roy, D.P., Vermote, E., Masek, J., Kovalskyy, V., 2012. Continental-scale validation of MODIS-based and LEDAPS Landsat ETM+ atmospheric correction methods. Remote Sens. Environ. 122, 175–184.
Kesel, R.H., 1989. The role of the Mississippi River in wetland loss in southeastern Louisiana, USA. Environ. Geol. Water Sci. 13, 183–193.
Keshava, N., 2003. A survey of spectral unmixing algorithms. Lincoln Lab. J. 14, 55–78.
Keshava, N., Mustard, J.F., 2002. Spectral unmixing. IEEE Signal Process. Mag. 19, 44–57.
Kindlmann, P., Burel, F., 2008. Connectivity measures: a review. Landsc. Ecol. 23, 879–890.
Kuleli, T., Guneroglu, A., Karsli, F., Dihkan, M., 2011. Automatic detection of shoreline change on coastal Ramsar wetlands of Turkey. Ocean Eng. 38, 1141–1149.
Lam, N.S.-N., Cheng, W., Zou, L., Cai, H., 2018. Effects of landscape fragmentation on land loss. Remote Sens. Environ. 209, 253–262.
Li, J., Roy, D.P., 2017. A global analysis of sentinel-2A, sentinel-2B and Landsat-8 data revisit intervals and implications for terrestrial monitoring. Remote Sens. 9, 902.
Lin, C., Wu, C.-C., Tsogt, K., Ouyang, Y.-C., Chang, C.-I., 2015. Effects of atmospheric correction and pansharpening on LULC classification accuracy using WorldView-2 imagery. Inform. Proces. Agricu. 2, 25–36.
Liu, T., Yang, X., 2013. Mapping vegetation in an urban area with stratified classification and multiple endmember spectral mixture analysis. Remote Sens. Environ. 133, 251–264.
Loreau, M., MOuquet, N., Holt, R.D., 2003. Meta-ecosystems: a theoretical framework for a spatial ecosystem ecology. Ecol. Lett. 6, 673–679.
Lu, D., Weng, Q., 2007. A survey of image classification methods and techniques for improving classification performance. Int. J. Remote Sens. 28, 823–870.
Luck, M., Wu, J., 2002. A gradient analysis of urban landscape pattern: a case study from the Phoenix metropolitan region, Arizona, USA. Landsc. Ecol. 17, 327–339.
Marleau, J.N., Guichard, F., Loreau, M., 2014. Meta-ecosystem dynamics and functioning on finite spatial networks. Proc. R. Soc. B Biol. Sci. 281, 20132094.
McKee, K.L., Cherry, J.A., 2009. Hurricane Katrina sediment slowed elevation loss in subsiding brackish marshes of the Mississippi River delta. Wetlands 29, 2–15.
Miller, R.L., Fram, M., Fujii, R., Wheeler, G., 2008. Subsidence reversal in a re-established wetland in the Sacramento-san Joaquin Delta, California, USA. In: San Francisco Estuary and Watershed Science. 6.
Morgan, J.P., 1972. Impact of subsidence and erosion on Louisiana coastal marshes and estuaries. In: Proceedings of the Coastal Marsh and Estuary Management Symposium. Division of Continuing Education. Louisiana State University, Baton Rouge, La, pp. 217–233.
Morton, R.A., 2003. An Overview of Coastal Land Loss: With Emphasis on the Southeastern United States. Citeseer.

Nagendra, H., Munroe, D.K., Southworth, J., 2004. From Pattern to Process: Landscape Fragmentation and the Analysis of Land Use/Land Cover Change. Elsevier.
Nath, S.S., Mishra, G., Kar, J., Chakraborty, S., Dey, N., 2014. A survey of image classification methods and techniques. In: Control, Instrumentation, Communication and Computational Technologies (ICCICCT), 2014 International Conference On. IEEE, pp. 554–557.
Neel, M.C., McGarigal, K., Cushman, S.A., 2004. Behavior of class-level landscape metrics across gradients of class aggregation and area. Landsc. Ecol. 19, 435–455.
Newton, A., Carruthers, T.J., Icely, J., 2012. The coastal syndromes and hotspots on the coast. Estuar. Coast. Shelf Sci. 96, 39–47.
Nichol, J., Wong, M.S., 2007. Remote sensing of urban vegetation life form by spectral mixture analysis of high-resolution IKONOS satellite images. Int. J. Remote Sens. 28, 985–1000.
Nyman, J.A., DeLaune, R.D., 1999. Four potential impacts of global sea-level rise on coastal marsh stability. Curr. Top. Wetland Biogeochem. 3, 112–117.
Nyman, J.A., Carloss, M., DeLaune, R.D., Patrick Jr., W.H., 1994. Erosion rather than plant dieback as the mechanism of marsh loss in an estuarine marsh. Earth Surf. Process. Landf. 19, 69–84.
Olliver, E.A., Edmonds, D.A., 2017. Defining the ecogeomorphic succession of land building for freshwater, intertidal wetlands in wax Lake Delta, Louisiana. Estuar. Coast. Shelf Sci. 196, 45–57.
Ord, J.K., Getis, A., 1995. Local spatial autocorrelation statistics: distributional issues and an application. Geogr. Anal. 27, 286–306.
Ord, J.K., Getis, A., 2001. Testing for local spatial autocorrelation in the presence of global autocorrelation. J. Reg. Sci. 41, 411–432.
Ortiz, A.C., Roy, S., Edmonds, D.A., 2017. Land loss by pond expansion on the Mississippi River Delta plain. Geophys. Res. Lett. 44, 3635–3642.
Pekel, J.-F., Cottam, A., Gorelick, N., Belward, A.S., 2016. High-resolution mapping of global surface water and its long-term changes. Nature 540, 418.
Penland, S., Wayne, L., Britsch, L.D., Williams, S.J., Beall, A.D., Butterworth, V.C., 2000a. Process classification of coastal land loss between 1932 and 1990 in the Mississippi River delta plain, southeastern Louisiana.
Penland, S., Wayne, L., Britsch, L.D., Williams, S.J., Beall, A.D., Butterworth, V.C., 2000b. Geomorphic classification of coastal land loss between 1932 and 1990 in the Mississippi River Delta Plain, Southeastern Louisiana.
Renaud, F.G., Kuenzer, C., 2012. The Mekong Delta System: Interdisciplinary Analyses of a River Delta. Springer Science & Business Media.
Riitters, K.H., O'neill, R.V., Hunsaker, C.T., Wickham, J.D., Yankee, D.H., Timmins, S.P., Jones, K.B., Jackson, B.L., 1995. A factor analysis of landscape pattern and structure metrics. Landsc. Ecol. 10, 23–39.
Roy, D.P., Ju, J., Kline, K., Scaramuzza, P.L., Kovalskyy, V., Hansen, M., Loveland, T.R., Vermote, E., Zhang, C., 2010. Web-enabled Landsat data (WELD): Landsat ETM+ composited mosaics of the conterminous United States. Remote Sens. Environ. 114, 35–49.
Roy, D.P., Kovalskyy, V., Zhang, H.K., Vermote, E.F., Yan, L., Kumar, S.S., Egorov, A., 2016. Characterization of Landsat-7 to Landsat-8 reflective wavelength and normalized difference vegetation index continuity. Remote Sens. Environ. 185, 57–70.
Shelestov, A., Lavreniuk, M., Kussul, N., Novikov, A., Skakun, S., 2017. Exploring Google earth engine platform for big data processing: classification of multi-temporal satellite imagery for crop mapping. Front. Earth Sci. 5, 17.
Syvitski, J.P., Kettner, A.J., Overeem, I., Hutton, E.W., Hannon, M.T., Brakenridge, G.R., Day, J., Vörösmarty, C., Saito, Y., Giosan, L., 2009. Sinking deltas due to human activities. Nat. Geosci. 2, 681–686.
Tessler, Z.D., Vörösmarty, C.J., Grossberg, M., Gladkova, I., Aizenman, H., Syvitski, J.P.M., Foufoula-Georgiou, E., 2015. Profiling risk and sustainability in coastal deltas of the world. Science 349, 638–643.
Tischendorf, L., 2001. Can landscape indices predict ecological processes consistently? Landsc. Ecol. 16, 235–254.
Turner, M.G., 1989. Landscape ecology: the effect of pattern on process. Annu. Rev. Ecol. Syst. 20, 171–197.
Turner, R.E., Rao, Y.S., 1990. Relationships between wetland fragmentation and recent hydrologic changes in a deltaic coast. Estuar. Coasts 13, 272–281.
Turner, M.G., Romme, W.H., Gardner, R.H., O'Neill, R.V., Kratz, T.K., 1993. A revised concept of landscape equilibrium: disturbance and stability on scaled landscapes. Landsc. Ecol. 8, 213–227.
Turner, M.G., Gardner, R.H., O'neill, R.V., 2001. Landscape Ecology in Theory and Practice. Springer.
Uuemaa, E., Antrop, M., Roosaare, J., Marja, R., Mander, Ü., 2009. Landscape metrics and indices: an overview of their use in landscape research. Living Rev. Landscape Res. 3, 1–28.
Wells, J.T., 1996. Subsidence, sea-level rise, and wetland loss in the lower Mississippi River delta. In: Sea-Level Rise and Coastal Subsidence. Springer, pp. 281–311.
Wulder, M., Boots, B., 1998. Local spatial autocorrelation characteristics of remotely sensed imagery assessed with the Getis statistic. Int. J. Remote Sens. 19, 2223–2231.